

6.2 Shock Reflection by a Cylinder

The reflection of oblique shock waves is a non-linear problem which has been investigated by many workers. Four types of reflection have been observed for the flow of a plane shock over a two-dimensional straight wedge. These types of reflection, together with the year in which they were discovered, are: regular reflection (RR) – 1878; single Mach reflection (SMR) – 1878; complex Mach reflection (CMR) – 1945; double Mach reflection (DMR) – 1951. Since the discovery of DMR work has concentrated on establishing the correct transition criteria between the various reflections. The type of reflection depends on the Mach number of the incident shock, M_s , the angle of the wedge, θ_w , and the ratio of the specific heats for the fluid, γ . So to test hypotheses for transition, experiments have been performed in which M_s and γ are fixed but θ_w varies continuously [14, 5, 6]. We have used the AMR algorithm to simulate the experiment of Bryson & Gross [14]. Namely, the reflection of a plane shock, $M_s = 2.81$ and $\gamma = 1.4$, by a circular cylinder.

For this problem the shock initially meets the cylinder head on, this is analogous to the reflection from a 90° wedge, and RR ensues. But as the incident shock propagates up the cylinder so the reflecting angle of the surface decreases until there is a transition from RR to MR. The type of MR depends on the strength of the incident shock. Moreover, further transitions can occur and it is possible to have the sequence of events $RR \rightarrow DMR \rightarrow CMR \rightarrow SMR$. Our simulation was done in two parts. The first part determined the transition from RR to MR, while the second part continued the simulation beyond this transition point so as to be able to compare the numerical shock pattern with a Schlieren photograph taken from the experiment.

6.2.1 Transition from RR to MR

The experiment was performed for two Reynolds numbers which differed by a factor of 10. Since there were no discernible differences between the loci of the triple points for these two cases it is not unreasonable to assume that the transition from RR to MR can be modelled using the Euler equations. For our calculation we chose to integrate these equations using Roe's flux difference splitting scheme combined with the SUPERBEE limiter function. Additionally, since the flowfield for this problem is symmetric we chose to compute a solution for just one half of the flow domain. Plots are presented where density contours are shown for the top half of the flow domain, while the corresponding computational grid is shown reflected about the line of symmetry.

Three grid levels were used for the calculation, see figure 6.9. The grid at level 0 contained 90 by 45 cells, and the refinement factors, rI and rJ , for grid levels 1 and 2 were set to 5. Thus the grid at level 2 has the same resolution as a uniformly spaced mesh of 2250 by 1125 cells. The grid at level 0 was generated by a series of radial lines and concentric quarter-circles. The radial lines were placed at 1° intervals, while the radii for

the quarter-circles were chosen such that the far-field boundary was 1.75 diameter lengths from the centre of the cylinder, all grid cells having the same aspect ratio. Ordinarily, a mesh at level l inherits its geometry from the grid at level $l - 1$, see §2.2. However a slight modification was required for this calculation otherwise those grid nodes at levels 1 and 2 that should lie on the surface of the cylinder would in fact lie on a 360 sided polygon. Thus at grid level 2 there would be 25 mesh interfaces for each edge of the polygon. Consequently, where appropriate the co-ordinates for a grid node were adjusted in order to make it lie on the surface of the cylinder.

The calculation was started with the exact shock conditions. The density and pressure for the quiescent fluid were taken as unity and the appropriate post-shock conditions were calculated using the moving shock relationships given in appendix A. Those mesh cells that straddled the initial shock position were primed with an area weighted average of the pre- and post-shock states. Zero flux reflecting boundary conditions were applied along the line of symmetry and the surface of the cylinder, and extrapolation from the interior was used for the far-field boundary. Although parts of the far-field boundary were either under or over specified this had no adverse affect on the numerical results. Therefore it was not considered worthwhile to employ a more sophisticated procedure along this boundary.

Figures 6.10–6.13 show a sequence of density contours³ taken during the transition from RR to MR. The first signs of MR occur approximately 44.8° from the forward stagnation point, see figure 6.11. But at this stage in the calculation there is insufficient resolution to determine the type of MR, and it is not until the Mach stem reaches a point 54° from the forward stagnation point that the salient features of DMR are well resolved, see figure 6.13. Since it is impossible to detect MR if the Mach stem is shorter than the length of 1–2 mesh cells the numerical transition point will inevitably be larger than the actual transition point. Moreover, the coarser the mesh the larger the transition angle. For example, judging from figure 6.12, if our mesh cells had been twice as long then it is doubtful if MR would have been detected before a point 46° from the forward stagnation point. Because of the limitations of our computer resources we are not able to compute this test problem using finer and finer grids in an attempt to determine the limiting position for the transition point. However, extrapolation from our present results suggest this limiting position is unlikely to be lower than 43° .

It is difficult to determine the accuracy of our numerical result. First, Bryson & Gross merely state that the transition from RR to MR occurs somewhere between 40° and 50° of the forward stagnation point. This vagueness is indicative of the accuracy of their measurements. The relatively long exposure time that they used to take Schlieren photographs, $0.2\mu s$, suggests that the uncertainty in their measurements cannot be less than $\pm 3^\circ$. Second, since there is some dispute as to the correct criterion for transition to occur several semi-analytic predictions have been made. Ben-Dor & Takayama[6] give

³These are drawn at 2.5% intervals.

transition curves in the (M_s, θ_w) plane for these semi-analytic predictions. From these curves it can be seen that for $M_s = 2.81$ the *detachment* criterion of von Neumann gives the transition angle as 50.9° , while the predictions of Heilig and Itoh based on Whitham's shock ray theory give angles of 46.3° and 44.6° respectively. Third, the experimental results given by Ben-Dor & Takayama suggest transition occurs at just under 40° . They claim that their measurements are accurate to $\pm 0.3^\circ$, however the error in reproducing any given result will be larger than this, from the scatter of their results we estimate $\pm 1.5^\circ$. Nevertheless, their experimental results are probably the most reliable prediction for the transition angle. Given the observation that the transition angle can actually vary with the radius of the cylinder[6], it seems likely that the discrepancy between our calculation and experiment is due to a combination of real gas and viscous effects.

The determination of the criterion for transition from RR to MR remains an active research area and one in which the AMR algorithm could prove beneficial. In particular, it should be possible to perform a series of calculations using different mesh integrators in order to determine the sensitivity of the transition angle to viscous and real gas effects.

6.2.2 Beyond the Transition Point

For the second part of our simulation we had to coarsen the computational grid, but all other details of the calculation remained unchanged. Again three grid levels were used, see figure 6.14. The grid at level 0 contained 90 by 45 cells and the refinement factors, rI and rJ , for grid levels 1 and 2 were set to 4. Thus the grid at level 2 has the same resolution as a uniformly spaced mesh of 1440 by 720 cells. The grid at level 0 was generated by a series of radial lines and concentric semi-circles. The radial lines were placed at 2° intervals, while the radii for the semi-circles were chosen such that the far-field boundary was 3.5 diameter lengths from the centre of the cylinder, all grid cells having the same aspect ratio. For clarity, some plots show mesh outlines rather than mesh cells.

The comparative resolutions of the computational grids used for the two parts of our simulation may be gauged by comparing figure 6.13 with figure 6.15. Both figures show density contours when the incident shock is approximately 53° from the forward stagnation point. For the transition calculation there were some 18 cells to resolve the Mach stem, while now there are just 5 cells. As the flow continues to evolve so the Mach stem grows in length and the effective resolution of the calculation increases, compare figure 6.16 with figure 6.15. After the incident shock passes the crown of the cylinder the Mach stem starts to diffract around the cylinder. Shortly afterwards there is a transition from DMR to CMR. The salient features of CMR are shown clearly in figure 6.17. The simulation was terminated when the Mach stem had reached a point 5° from the rear stagnation point, see figure 6.18. At later times there is considerable separation of the flow from the surface of the cylinder, and since our calculation is inviscid this separation would not be modelled properly.

The precise moment of termination was chosen so as to be able to compare the overall flow pattern with experiment. Compare the density contours for our numerical results shown in figure 6.19 with the Schlieren photograph taken by Bryson & Gross shown in figure 6.20. The general agreement is excellent. The numerical resolution of the contact discontinuity and vortex are particularly impressive. Indeed, the computational results for this test problem that are available in the literature, for example Yang *et al*[73], simply fail to resolve these features. Unfortunately, the resolution of the Schlieren photograph is insufficient to determine whether the suggestion of roll-up along the contact discontinuity is correct or not. However, since we have ignored viscous effects some differences would not be unexpected.

6.2.3 Comment

In this section we have tried to demonstrate that the AMR algorithm has the potential to be used as a serious research tool. Inevitably, the deeper one delves into a particular problem the larger the uncertainties become and the more difficult it is to apportion the discrepancy between computation and experiment. For in general, discrepancies can arise because of: inadequacies of the fluid model, insufficient grid resolution, poor numerical schemes, coding errors, poor experimental technique, obtrusive measuring, incorrect interpretation of results, . . . ; the list is endless. However, of one thing we are certain. Any fine tuning of the AMR algorithm will have to be done in tandem with an experimental group, a point to which we shall return later.

Finally, in keeping with the aim of this section we have not given any statistics for the computational grid or the run times for the two parts of our simulation. Suffice it to say, both calculations were performed on a Sun SPARCstation 1 with 8 Mbytes of core memory and took less than 1 day to run. Furthermore, no user intervention was required between the start and finish of each simulation.

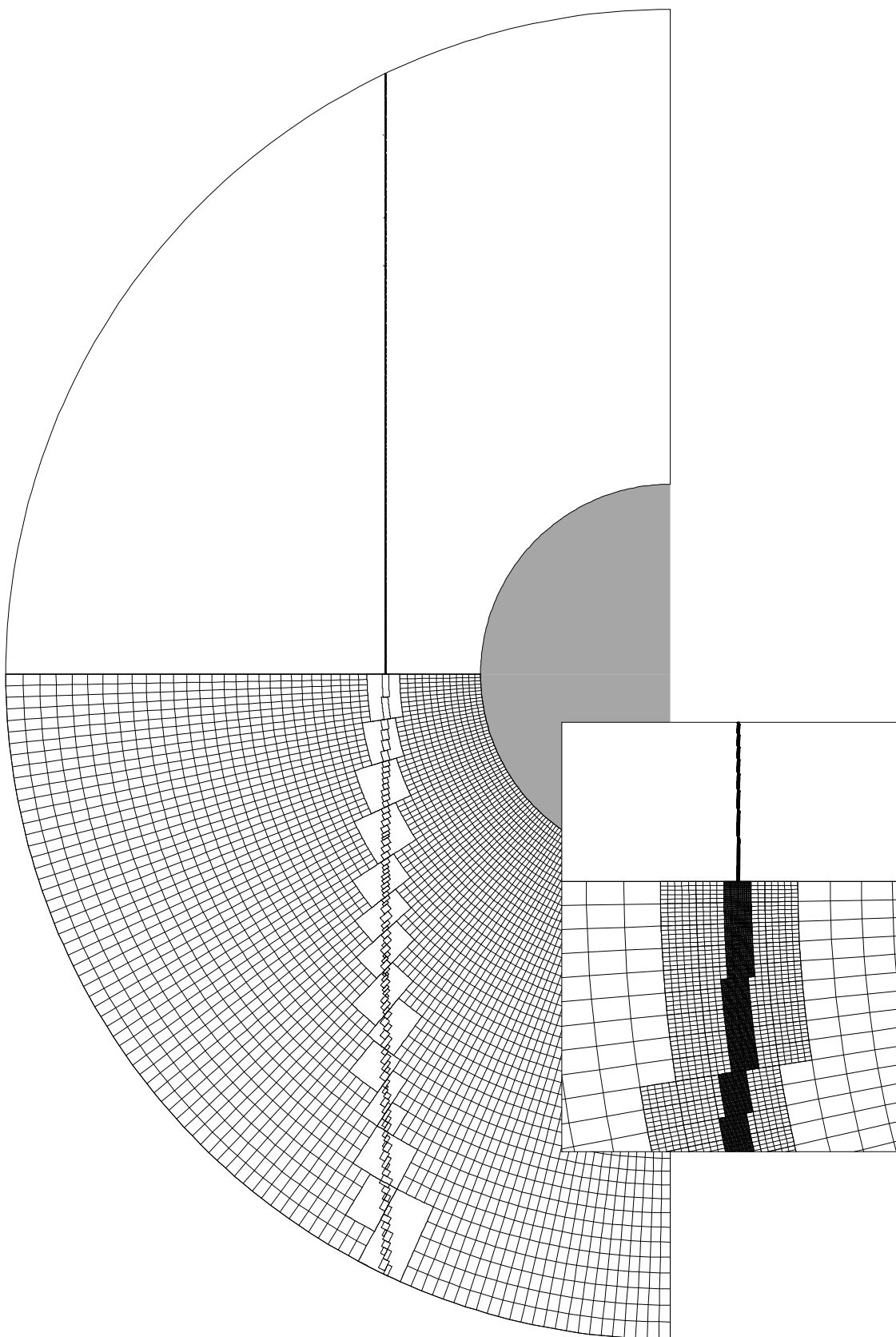


Figure 6.9: Initial conditions for the calculation $RR \rightarrow MR$.

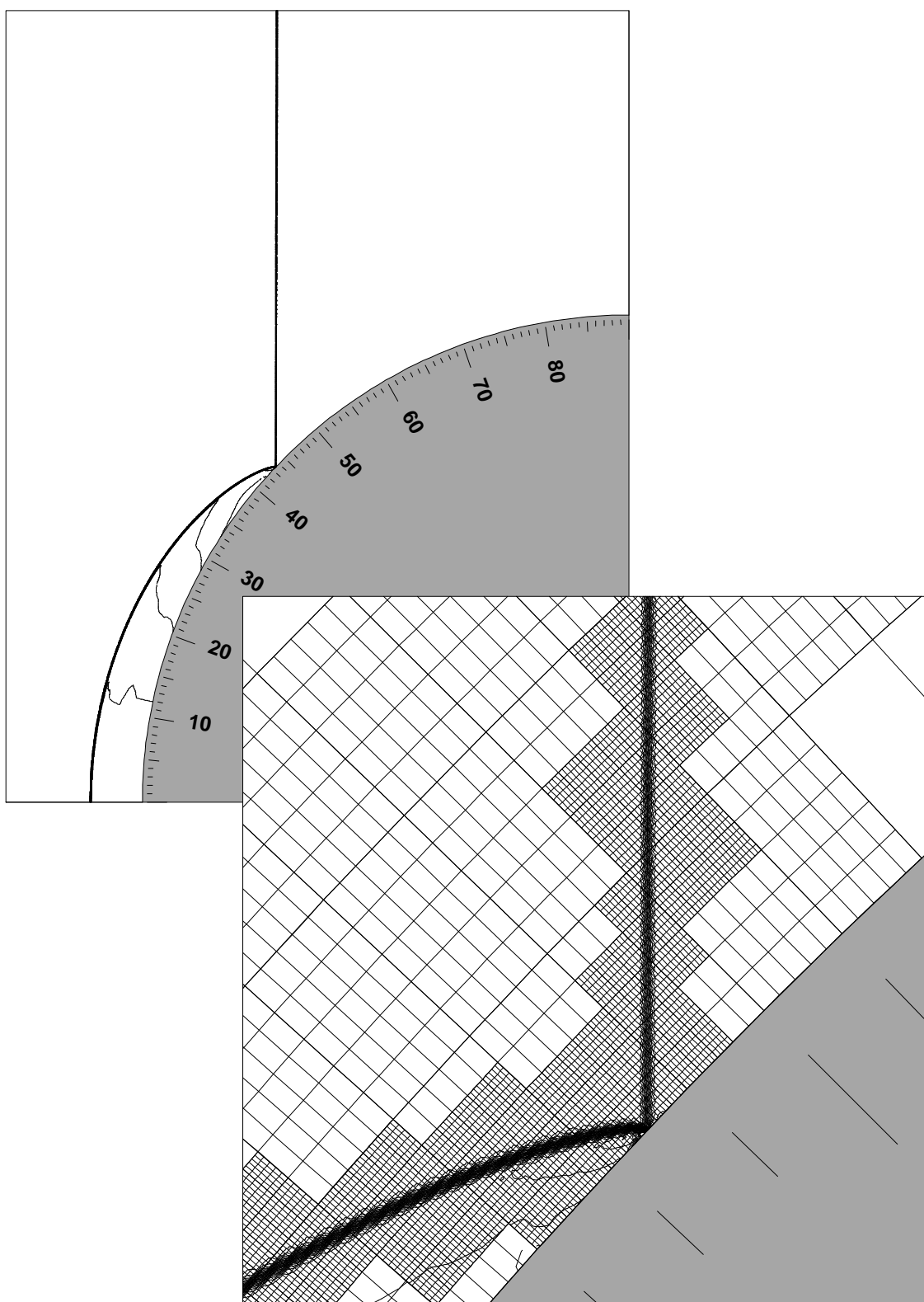


Figure 6.10: RR occurs before the transition point.

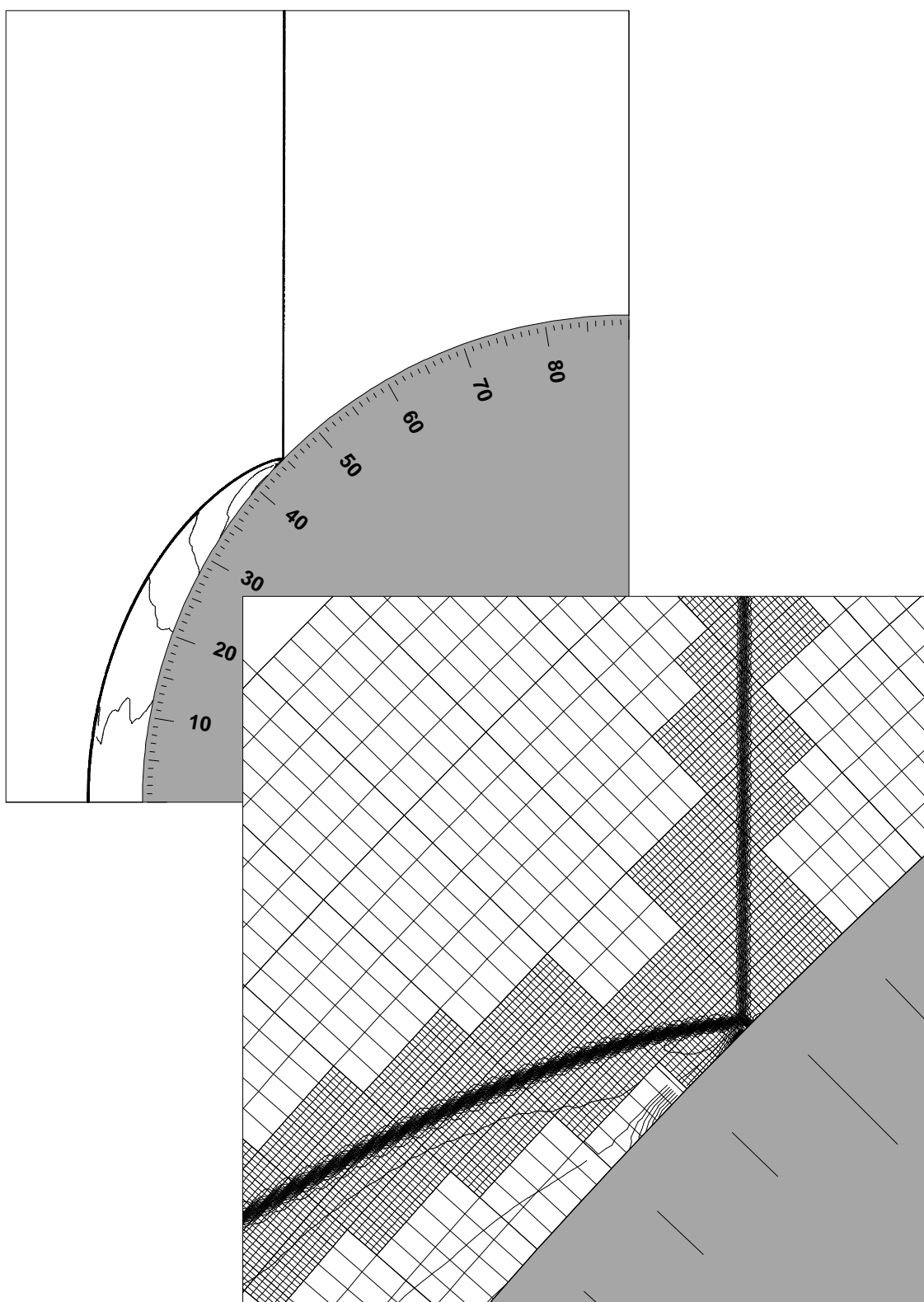


Figure 6.11: The earliest signs of MR.

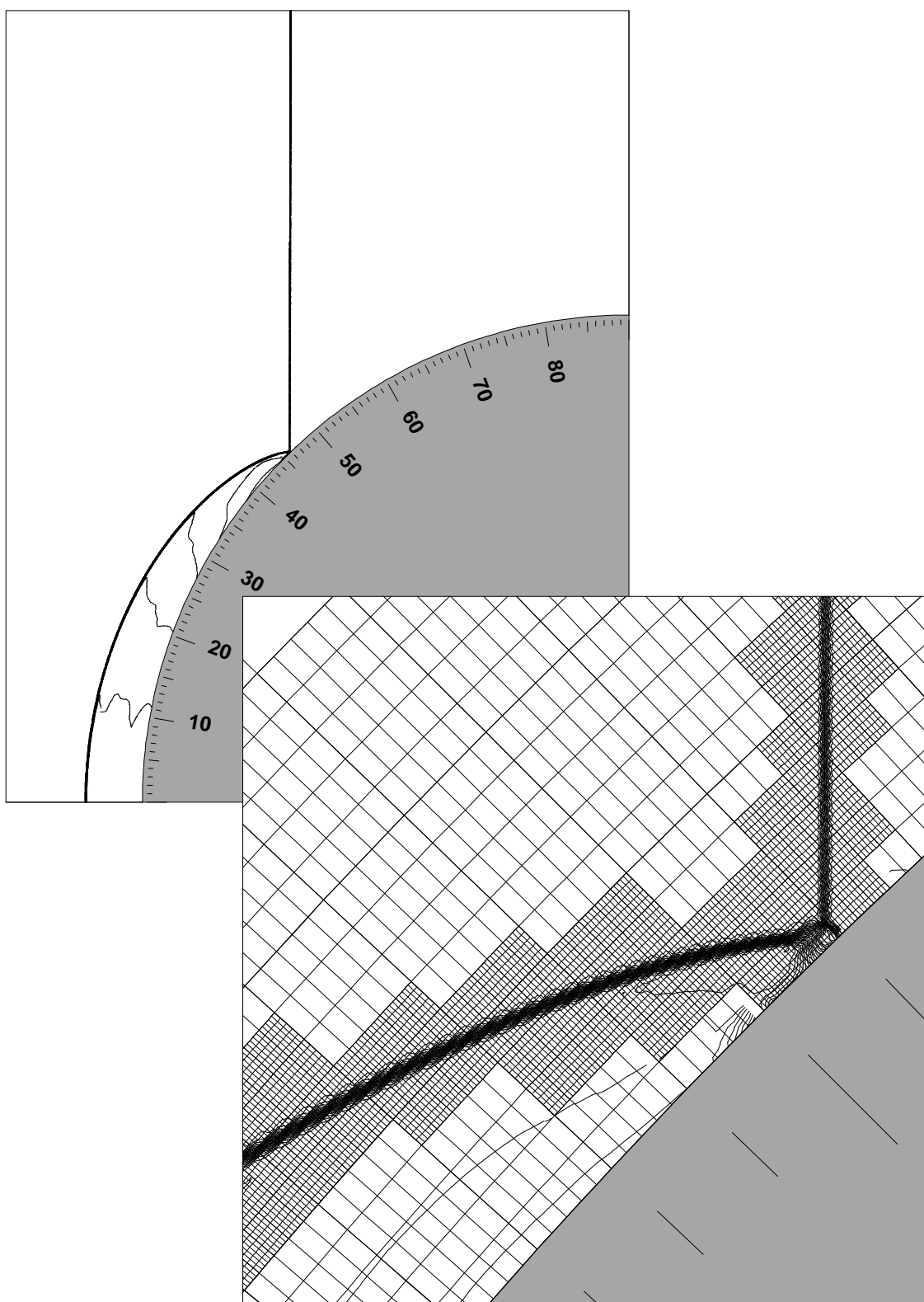


Figure 6.12: Confirmation that transition has occurred.

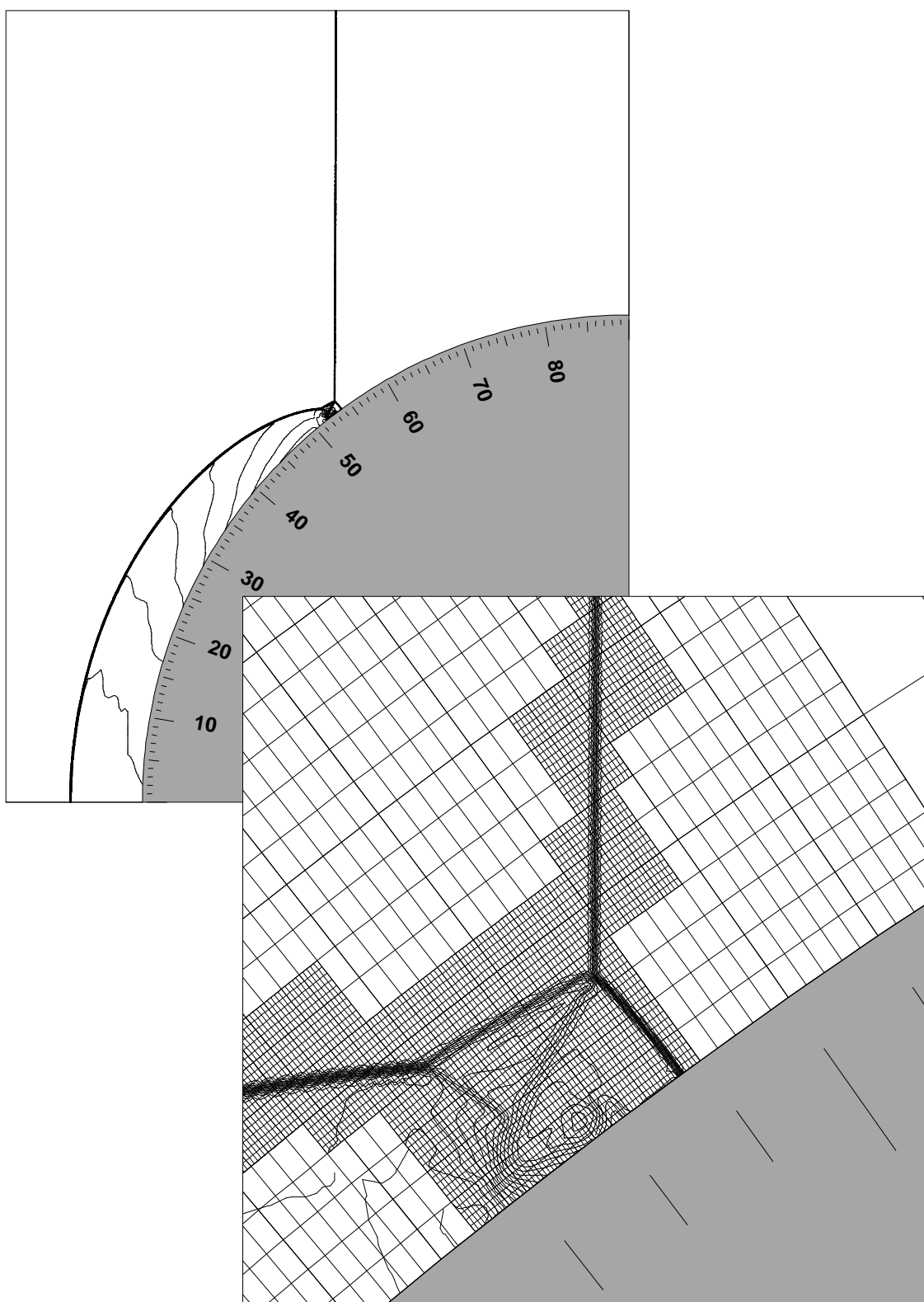


Figure 6.13: DMR occurs after the transition point.

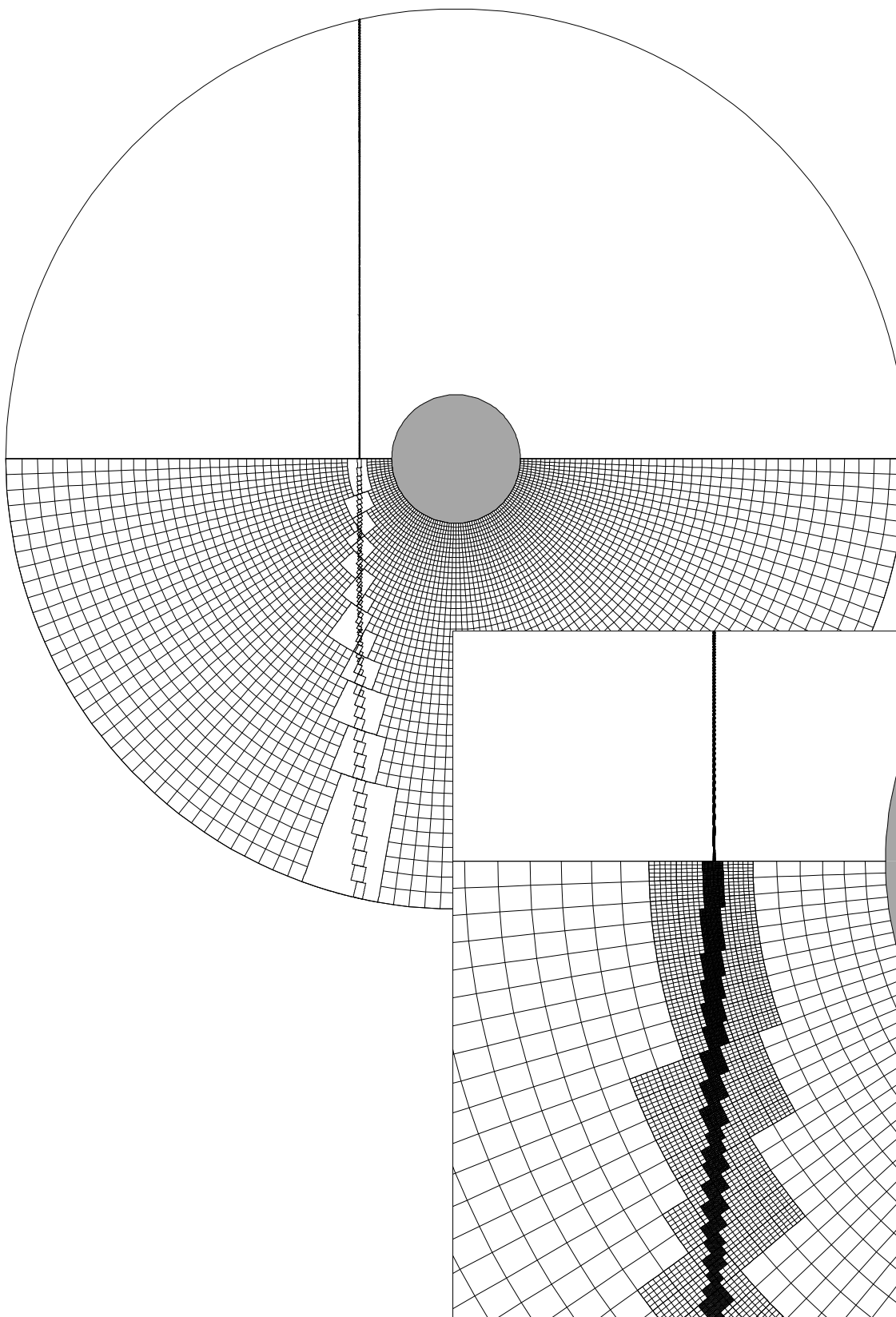


Figure 6.14: Initial conditions for part two of the simulation.

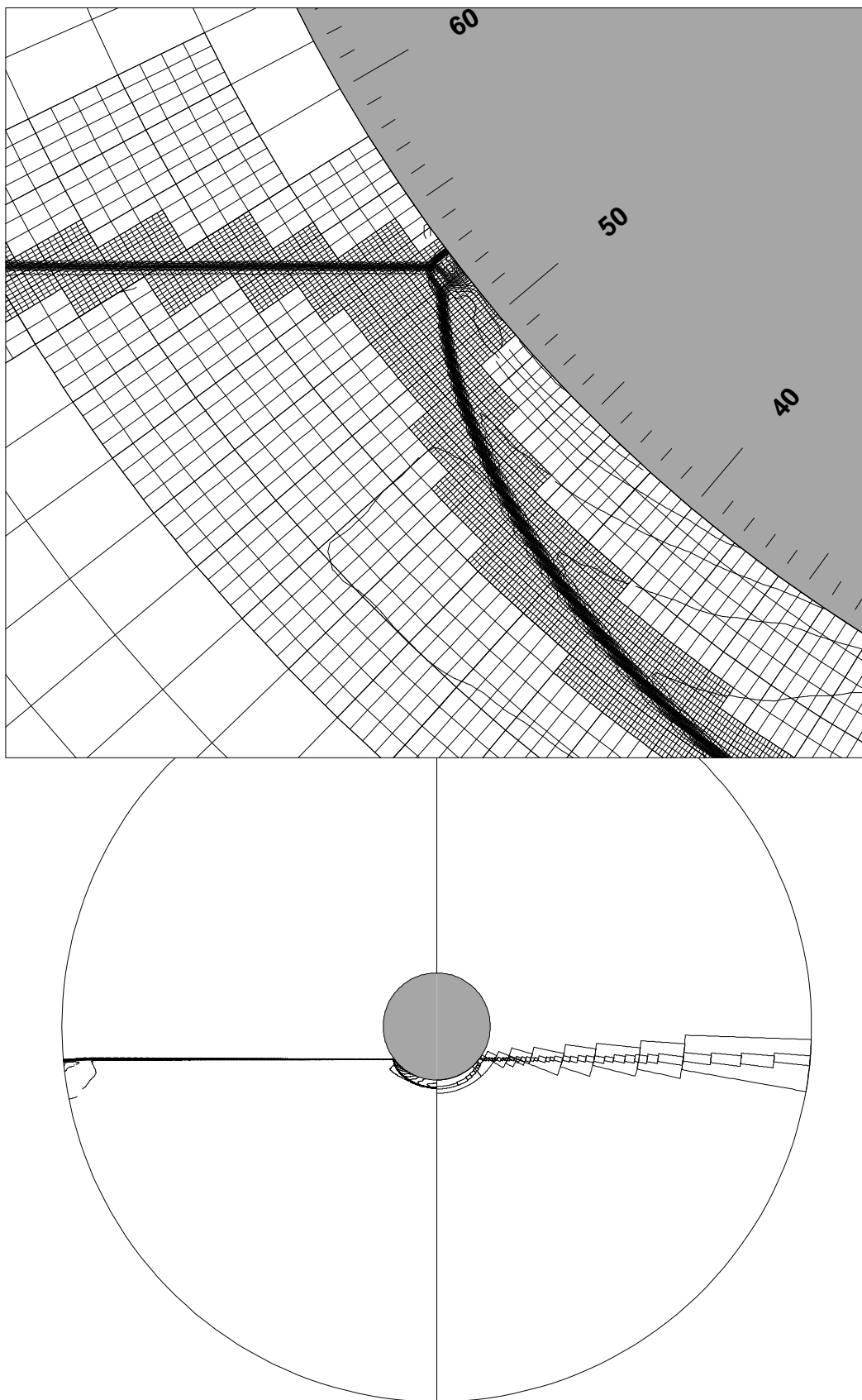


Figure 6.15: A coarser grid was used for part two of the simulation, cf. figure 6.13.

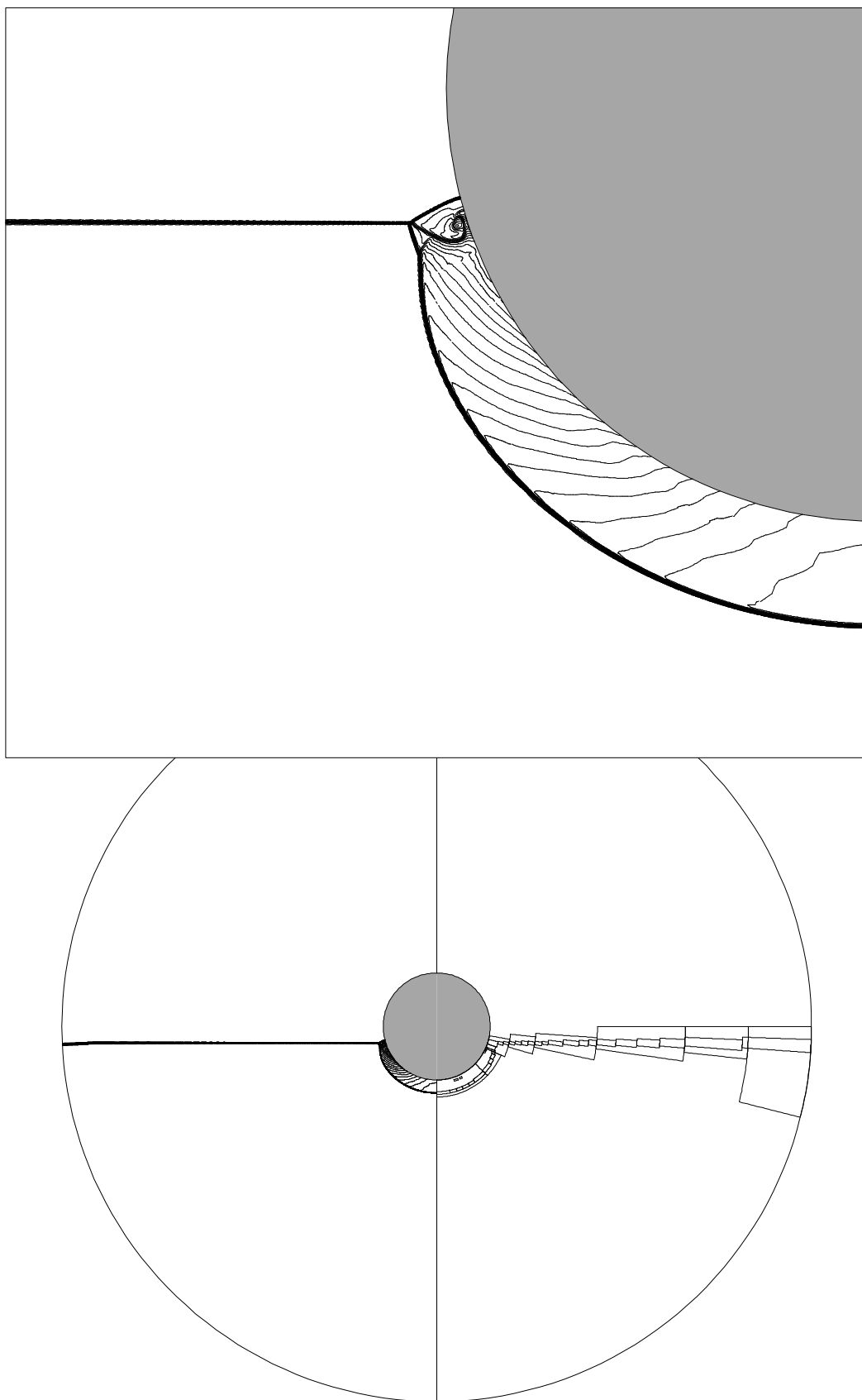


Figure 6.16: As the Mach stem grows so the effective resolution increases.

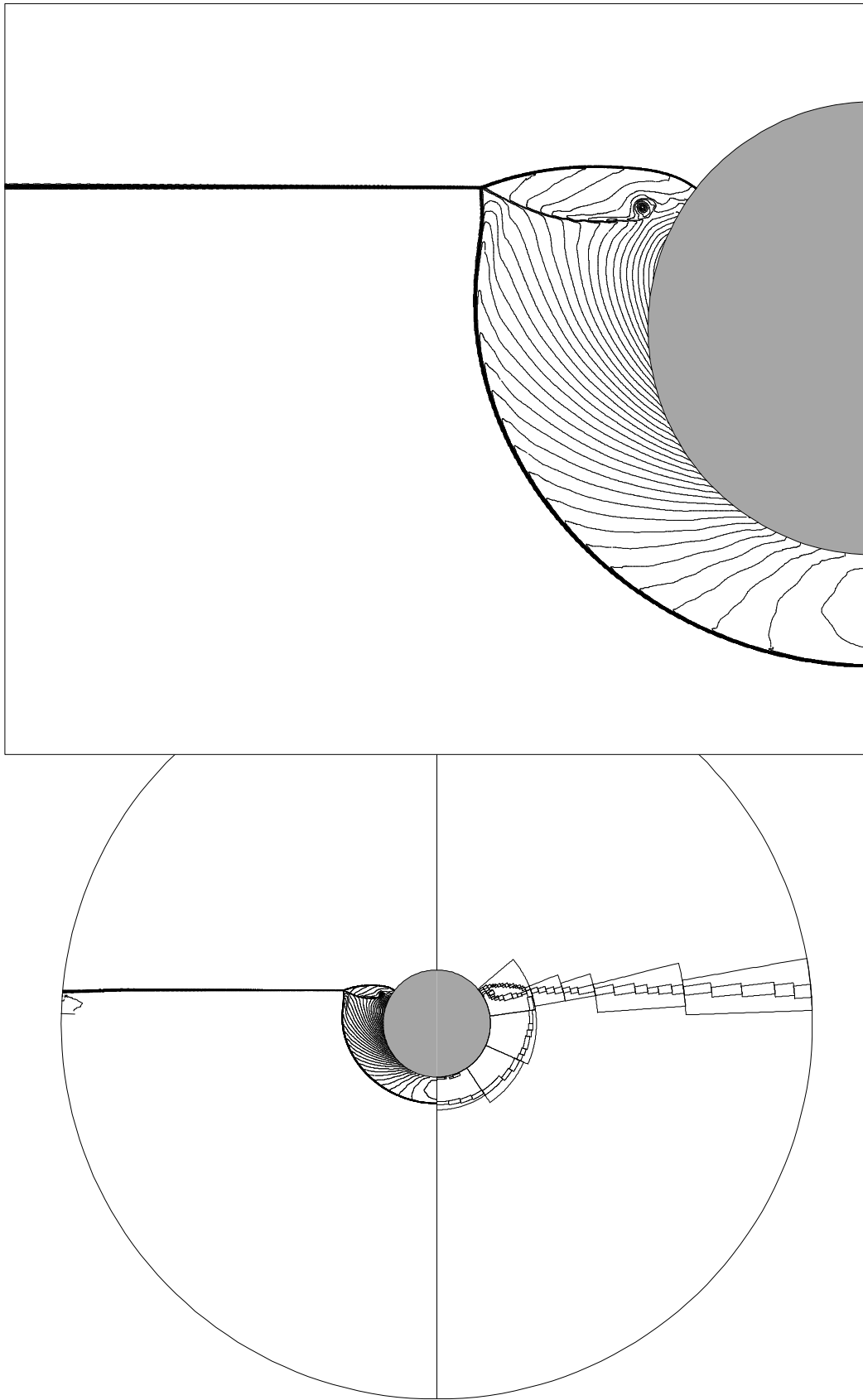


Figure 6.17: Transition from DMR to CMR has occurred.

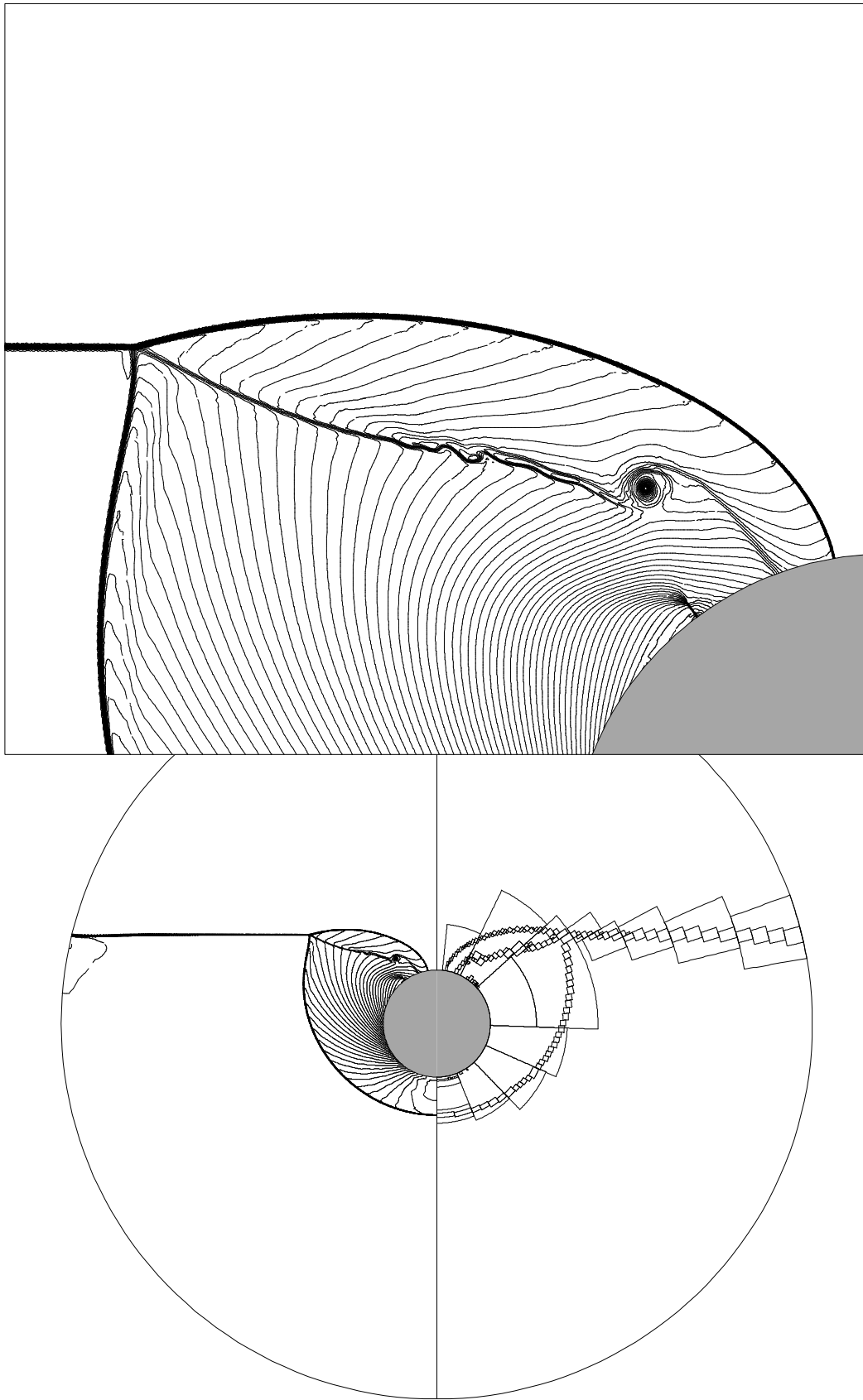


Figure 6.18: The Mach stem has diffracted around the cylinder.

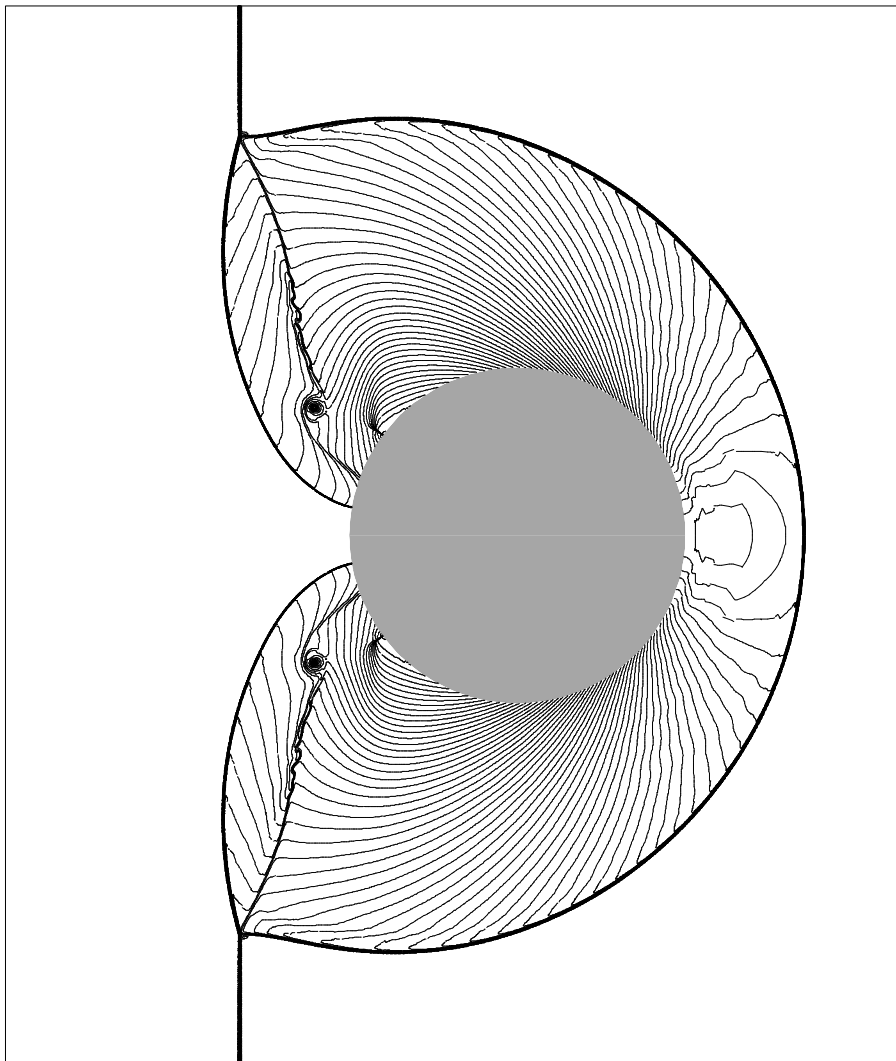


Figure 6.19: Density contours at the end of the simulation, cf. figure 6.20.

Figure 6.20: Schlieren photograph taken by Bryson & Gross[14], cf. figure 6.19. Key: I.S., incident shock; R.S., reflected shock; M.S., Mach stem; C.D., contact discontinuity; V, vortex; T.P., triple point.